ACCOUNTS
of chemical research

Mixed Frequency-/Time-Domain Coherent Multidimensional Spectroscopy: Research Tool or Potential Analytical Method?

ANDREI V. PAKOULEV, MARK A. RICKARD, KATHRYN M. KORNAU, NATHAN A. MATHEW, LENA A. YURS, STEPHEN B. BLOCK, AND JOHN C. WRIGHT*

Department of Chemistry, University of Wisconsin, Madison, Wisconsin 53706

RECEIVED ON JANUARY 23, 2009

CONSPECTUS

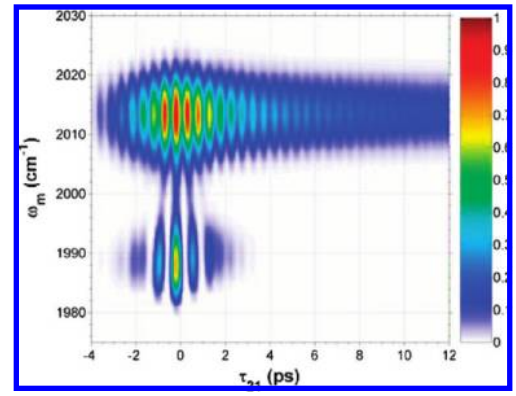

Coherent multidimensional spectroscopy (CMDS) is now the optical analogue of nuclear magnetic resonance (NMR). Just as NMR heteronuclear multiple-quantum coherence (HMQC) methods rely on multiple quantum coherences, achieving widespread application requires that CMDS also excites multiple quantum coherences over a wide range of quantum state energies. This Account focuses on frequency-domain CMDS because these methods tune the excitation frequencies to resonance with the desired quantum states and can form multiple quantum coherences between states with very different energies.

CMDS methods use multiple excitation pulses to excite multiple quantum states within their dephasing time, so their quantum mechanical phase is maintained. Coherences formed from pairs of the excited states emit coherent beams of light. The temporal ordering of the excitation pulses defines a sequence of coherences that can result in zero, single, double, or higher order coherences as required for multiple quantum coherence CMDS. Defining the temporal ordering and the excitation frequencies and spectrally resolving the output frequency also defines a particular temporal pathway for the coherences, just as an NMR pulse sequence defines an NMR method. Two dimensional contour plots through this multidimensional parameter space allow visualization of the state energies and dynamics.

This Account uses nickel and rhodium chelates as models for understanding mixed frequency-/time-domain CMDS. Mixed frequency-/time-domain methods use excitation pulse widths that are comparable to the dephasing times, so multidimensional spectra are obtained by scanning the excitation frequencies, while the coherence and population dynamics are obtained by scanning the time delays. Changing the time delays changes the peaks in the 2D excitation spectra depending upon whether the pulse sequence excites zero, single, or double quantum coherences. In addition, peaks split as a result of the frequency-domain manifestation of quantum beating. Similarly, changing the excitation and monochromator frequencies changes the dependence on the excitation delay times depending upon whether the frequencies match the resonances involved in the different time-ordered pathways. Contour plots that change a time delay and frequency visualize the temporal changes of specific spectral features.

Frequency-domain methods are resonant with specific states, so the sequence of coherences and populations is defined. Coherence transfer, however, can cause output beams at unexpected frequencies. Coherence transfer occurs when the thermal bath induces a coherence between two states (a and g) to evolve to a new coherence (b and g). Since the two coherences have different frequencies and since there are different time orderings for the occurrence of coherence transfer, the delay time dependence develops modulations that depend on the coherences' frequency difference.

Higher order coherences can also be generated by raising the excitation intensities. New features appear in the 2D spectra and dynamic Stark splittings occur. These effects will form the basis for the higher order multiple quantum coherence methods and also provide a method for probing molecular potential energy surfaces.

Published on the Web 05/15/2009 www.pubs.acs.org/acr
10.1021/ar900032g CCC: $71.50

Introduction

Spectroscopy forms the heart of the analytical methodology used for routine chemical measurement. Of all the analytical spectroscopic methods, NMR spectroscopy is unique in its ability to correlate spin resonances and resolve spectral features from spectra containing thousands of peaks. For example, heteronuclear multiple quantum coherence (HMQC) spectroscopy achieves this capability by exciting ^{1}H, ^{15}N, ^{13}C═O, and ^{13}Cα spins to form a multiple quantum coherence characteristic of a specific position in a protein's backbone.[1] Three excitations define a specific residue, and a fourth defines the coupling to an adjacent residue. Not only does it decongest the spectra, it defines the couplings and connectivity between the different nuclear spin states. Coherent multidimensional spectroscopy (CMDS) has emerged as the optical analogue of nuclear magnetic resonance (NMR), and there is great interest in using it as a general analytical methodology.[2−4] If CMDS is to have widespread use as an analytical technique, it is important to develop similar multiple quantum coherence methods.

CMDS divides into time- and frequency-domain methods. Time-domain methods dominate NMR and CMDS experiments.[3,5−10] Unlike time-domain NMR, the bandwidth of time-domain CMDS does not cover the range of interesting transitions. However, if a pathway contains a population, the first and last coherences are independent.[11] These pathways are not fully coherent and are sensitive to population relaxation effects where new transitions appear in the spectra from populations in unknown states.[12]

Frequency-domain methods do not have the same constraints and can use multiple quantum coherence pathways with states having disparate energies.[2] There is therefore interest in developing these methods as a general analytical methodology. We will use our work in coherent multidimensional vibrational spectroscopy (CMDVS) to describe the basic fundamentals of CMDS methods and provide model examples of their current capabilities. However, frequency-domain CMDS approaches can provide the same capabilities for any combination of electronic, vibrational, or rotational quantum states.

Background

CMDS developed from the multiresonant, nonlinear spectroscopies of coherent Raman spectroscopy.[13] CMDS creates quantum mechanical superposition states by a successive series of resonant electromagnetic field interactions.[5] N interactions that mix N quantum states with the ground state, g, create a time-dependent superposition state, $\Psi = \sum_{m=0}^{N}\psi_m(x,y)e^{i\vec{k}_m\cdot\vec{z}-(i\omega_m-\Gamma_m)t}$, which oscillates at $\omega_{nm} \equiv \omega_n - \omega_m$. Each mn pair is a coherence described by the ket and bra, $|m\rangle\langle n|$. Their oscillations create coherent, directional light beams whose intensity maximizes when $\vec{k}_{\text{signal}} = \sum\vec{k}_n$ ($\vec{k}_n$ is the wave vector of the nth beam). Since CMDS depends upon creating multiple excitations while the states remain phase coherent, the excitation intensities must create excitation rates that are fast compared with the dephasing rate, Γ. The sequence of coherences define a coherence pathway. For example,

$$gg \xrightarrow{1} gb \xrightarrow{2} cb \xrightarrow{3} db$$

specifies the temporal evolution of the ket and bra states of a fully coherent pathway; $gg \rightarrow gb \rightarrow bb \rightarrow bg$ is not fully coherent because bb is a population. Coherences depend on the difference in the number of excited states in the ket and bra.[3] If states a and b are vibrational fundamental modes, then coherences such as ba, ag, and $(b+a,g)$ are zero, single, and double quantum coherences, respectively (Of course, a or b could be combination band or overtone states. For example, if b is a combination band involving two modes and a is a fundamental, then $(b,2a)$, ba, bg, $(a+b,g)$ would be zero, single, double, and triple quantum coherences, respectively.).

In frequency-domain CMDS, the excitation is long compared with the dephasing time, the superposition state reaches a steady state, and the output coherence is driven by the fields. Spectra are acquired by measuring the intensity while scanning the excitation frequencies. In time-domain CMDS, the excitation is impulsive, and the output coherence radiates by free induction decay (FID). Spectra are acquired by measuring the intensity while scanning the delay time to define the phase oscillations and then Fourier transforming the data to obtain a spectrum. For mixed frequency-/time-domain methods, the excitation is comparable to the dephasing rate, and both the driven and FID processes contribute. Spectra are acquired by scanning the excitation frequencies for fixed time delays, while temporal relaxation is measured by scanning the time delay for fixed frequencies.

Time-domain spectroscopy requires phase coherence while the time delays change.[3] It is achieved by generating multiple pulses from a single pulse.[8,14,15] The frequency range is defined by the pulse bandwidth, typically 150−200 cm^{-1}. Since fully coherent pathways require phase coherence during the entire nonlinear process, it will be difficult to use fully coherent time-domain methods over wide frequency ranges. Frequency-domain spectroscopy requires only short-term phase coherence over the dephasing time, so each pulse can have different frequencies, and the frequency range can be wide.

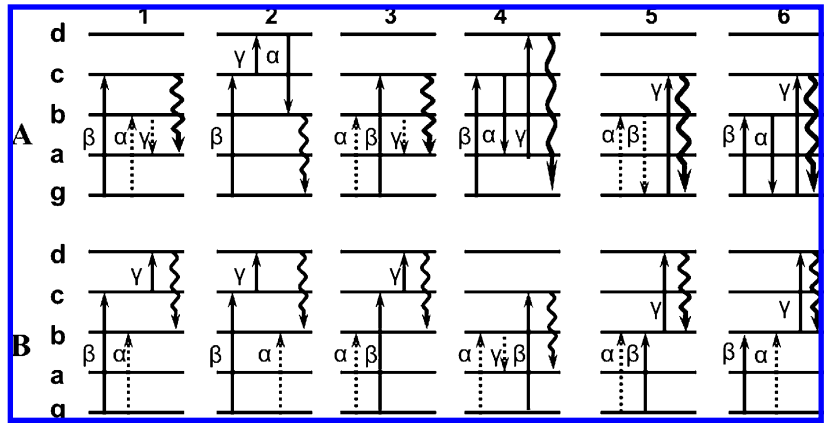

FIGURE 1. Example WMEL diagrams that show the resonances for three excitation frequencies.[16] Letters represent single states, Greek letters represent excitation frequency for $\vec{k}_{\text{signal}} = -\vec{k}_\alpha + \vec{k}_\beta + \vec{k}_\gamma$, solid and dotted arrows show ket and bra transitions, and a wavy arrow shows the signal. Time evolves from left to right.

Wave mixing energy level (WMEL)[16] diagrams define the coherence pathways and their resonances. Figure 1 shows the fully resonant WMEL diagrams assuming the phase matching condition $\vec{k}_{\text{signal}} = -\vec{k}_\alpha + \vec{k}_\beta + \vec{k}_\gamma$. Columns 1−4 show the eight fully coherent pathways (the Mukamel pathways R1−R4 are also special cases of the pathways).[17] Columns 5 and 6 show four special cases that have an intermediate population and correspond to the two-color pump−probe pathways of ultrafast spectroscopy.[18] The solid and dotted arrows represent transitions on the coherence's ket and bra parts, respectively. As an example, pathway 3A represents the temporal evolution

$$gg \xrightarrow{\alpha} gb \xrightarrow{\beta} cb \xrightarrow{\gamma} ca$$

where *ca* emits the observed signal.

Each pathway has different characteristics.[5,13] Columns 1−4 measure coherent processes, while columns 5 and 6 involve populations and measure incoherent processes. The intermediate coherences after the first two interactions are zero quantum coherences for the pathways in columns 1 and 3, double quantum coherences in column 2, single quantum coherences in column 4, and populations in columns 5 and 6. The pathways also differ in whether the system gains energy from the interactions with the electromagnetic fields. Nonparametric pathways deposit energy in the system because the final coherence emission does not return the system to its initial state. Figure 1A is a nonparametric process, while pathway 2A is a parametric process.

The final coherences from different pathways are additive and constructively or destructively interfere.[5,13] The sign of a coherence depends upon whether the number of bra-side interactions is odd or even. For example, the first two interactions in rows A and B are identical for columns 1−3 in Figure 1, but the third interactions differ, so the two rows have opposite signs and destructively interfere. Cross-peaks will not be observed if the frequencies and dephasing rates are identical. Intra- or intermolecular interactions anharmonically couple the states, and the interference is incomplete.[19]

Frequency-Domain CMDS

The first CMDS experiments were frequency-domain coherent anti-Stokes Raman spectroscopy (CARS), multiply enhanced parametric spectroscopy (MEPS), multiply enhanced nonparametric spectroscopy (MENS), and coherent Stokes Raman spectroscopy (CSRS).[13,20,21] These methods were fully coherent and provided line-narrowing and mode-coupling information. However, they involved electronic transitions and required cryogenic temperatures to achieve the selectivity. Working at room temperature required developing vibrational CMDS. Ivanecky and Wright attempted extending the four-wave mixing (FWM) methods to six-wave mixing (SWM) where two vibrational modes could be excited by Raman processes.[22] However, cascaded FWM processes obscured the SWM signal. Instead, the Wright group used infrared transitions that directly accessed the vibrational levels to create a new family of frequency-domain coherent methods.[23,24] This approach resulted in doubly vibrationally enhanced (DOVE) FWM, a fully coherent two-dimensional vibrational spectroscopy.[25−27] DOVE FWM uses one Raman and two infrared transitions. Cross-peaks depend upon anharmonic creation of combination band or overtone transitions. Later work extended DOVE FWM to the mixed frequency-/time-domain DOVE FWM,[28] so one could isolate specific coherence pathways by defining the temporal ordering of the excitation pulses and use the inter-

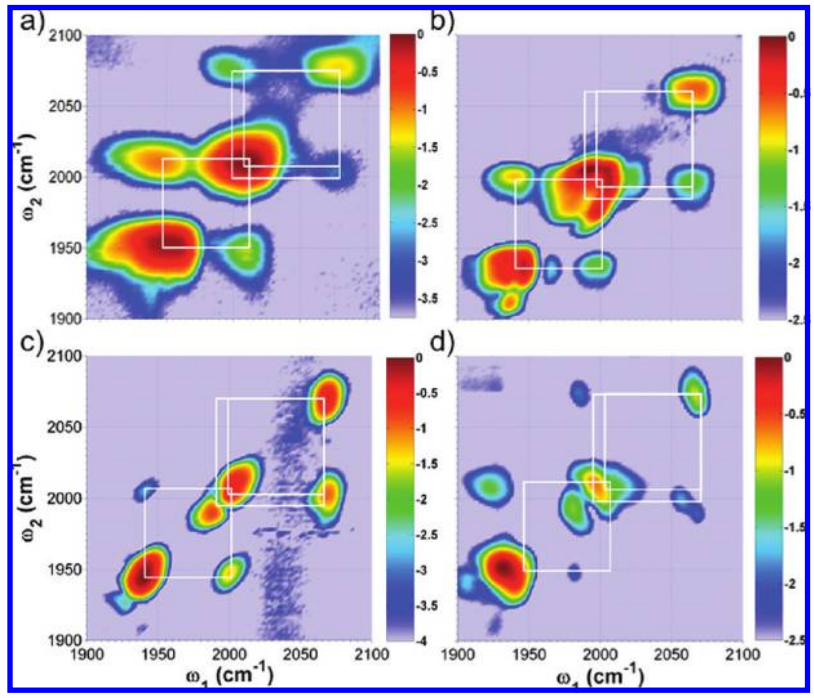

FIGURE 2. Representative TRIVE FWM 2D spectra of $Ni(CO)_2$/ $Ni(CO)_3$ scanning excitation frequencies with (τ_{21}, $\tau_{2'1}$) values of (a) (0,0), (b) (2,1), (c) (2,1), and (d) (−1,2) ps. For panel a, there was no monochromator; for panels b, c, and d, $\omega_m = \omega_1$. Boxes define vibrational energies of $Ni(CO)_2$ and $Ni(CO)_3$ (table 1).

ference between the different pathways to coherently control the relative peak intensities.[29]

The next method in the new family was triply vibrationally enhanced (TRIVE) FWM.[30] TRIVE FWM uses four infrared transitions and all the pathways in Figure 1. Cross-peaks occur because anharmonic coupling removes the destructive interference between parametric and nonparametric pathways.[19] Meyer et al. demonstrated that adding a monochromator to spectrally resolve the output signal allowed selection of individual pathways and improved the resolution of TRIVE FWM.[31] This Account uses TRIVE FWM to illustrate mixed frequency-/time-domain CMDS methods.

Example CMDS Results: Two-Dimensional Spectra

We define the frequency, wavevector, and temporal position of the *i*th excitation pulse by ω_i, $\vec{k}_i$, and τ_i, respectively, and the delay time between two pulses by $\tau_{ij} \equiv \tau_i - \tau_j$. Figure 2 shows examples of $Ni(CO)_2$ and $Ni(CO)_3$ (triphenylphosphine dicarbonyl nickel and diphenylphosphine tricarbonyl nickel) TRIVE FWM 2D spectra using the phase matching $\vec{k}_{signal} = \vec{k}_1 - \vec{k}_2 + \vec{k}_{2'}$ and scanning the ω_1 and ω_2 frequencies while measuring the output intensity. Table 1 summarizes their vibrational modes. The intensity scale is logarithmic, so one can observe all of the features over a wide dynamic range. Figure 2a shows the 2D spectrum when the beams are temporally overlapped and the output signal is not spectrally resolved. It contains contributions from all 12 coherence pathways in Figure 1. The three boxes indicate the diagonal and cross peak positions of the $Ni(CO)_2$ (lower left) and $Ni(CO)_3$ (two upper right) vibrational transitions. The figure also has unresolved overtone and combination bands (e.g., pathways 2A, 1−3B, and 5,6B). Figure 2b shows the same spectrum but with time delays for time orderings 1A,B in Figure 1. The time delays eliminate other pathways and isolate pathways 1A and 1B. Figure 2c shows the same spectrum as Figure 2b, but a monochromator now spectrally resolves the output signal. The monochromator is scanned so its frequency, $\omega_m = \omega_1$. Since the output from pathway 1B is anharmonically shifted from pathway 1A, this scan isolates the contributions from pathway 1A. Figure 2d shows the spectrum with $\omega_m = \omega_1$ and time delays that isolate pathway 2B. For our two-color experiments, the first and third resonances have the same frequency, ω_2, and the second resonance involves ω_1. Note that the peaks are shifted to the left from the boxes because $\omega_m = \omega_1$ is now resonant with combination band

TABLE 1

vibrational energies (cm^{-1})	$Ni(CO)_2$	$Ni(CO)_3$
a (asym stretch)	1943	1900
a' (asym stretch)		1999
b (sym stretch)	2002	2069
a + *b* (comb band)	3919	~4058

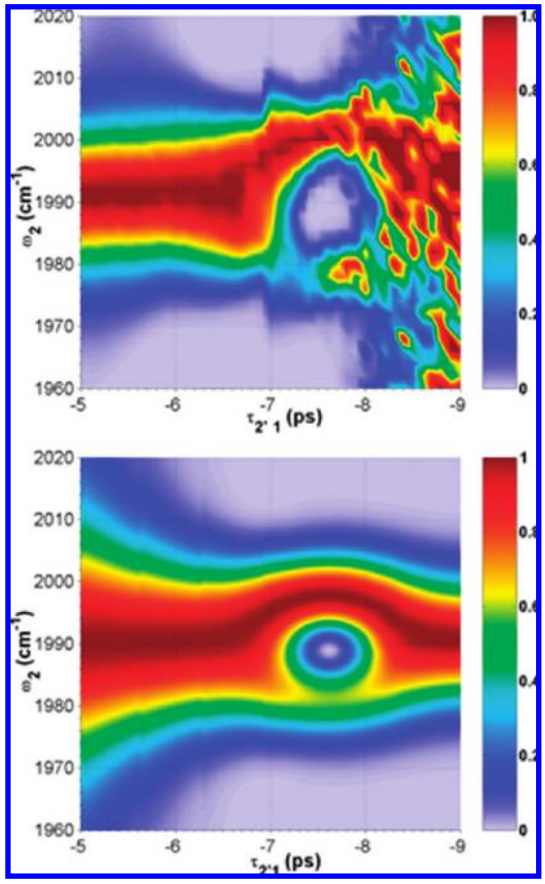

FIGURE 3. Experimental (top) and simulated (bottom) dependence of resonance when $\omega_1 = 2069$ cm^{-1}, $\tau_{21} = -5$ ps, and ω_2 and $\tau_{2'1}$ are scanned. Each vertical slice is normalized to most intense data point.[32] Reproduced with permission from ref 32. Copyright 2007 American Chemical Society.

and overtone transitions while ω_2 remains resonant with the fundamental modes.

Frequency-Domain Quantum Beating

The spectral region near $\omega_1 \approx \omega_2 = 2000$ cm^{-1} is complex because there are three unresolved vibrational modes from the two asymmetric $Ni(CO)_3$ modes and the symmetric $Ni(CO)_2$ mode that interfere at this frequency.[2,30] These modes all lie within the excitation pulse bandwidth, so they are not spectrally resolved. The coherences associated with each give rise to quantum beating. We showed that the frequency-domain manifestation of quantum beating is a periodic splitting of the diagonal and cross peaks as a function of the delay time.[32] This splitting appears in the diagonal peak of Figure 2c and the diagonal and cross peaks of Figure 2d.

The splitting is clearly seen in Figure 3 for the cross peak at $(\omega_1, \omega_2) = (2069, 1989)$ cm^{-1}.[32] The top spectrum shows the dependence when $\omega_1 = 2069$ cm^{-1}, $\tau_{2,1} = -5$ ps, and we vary ω_2 and $\tau_{2',1}$. These conditions isolate pathway 6A. The spectrum is normalized to have the same maximum intensity at each delay setting. The lower spectrum is a simulation based on a 9 cm^{-1} splitting between the two asymmetric modes of $Ni(CO)_3$. The asymmetry in the pattern results from the unequal intensity of the two transitions.

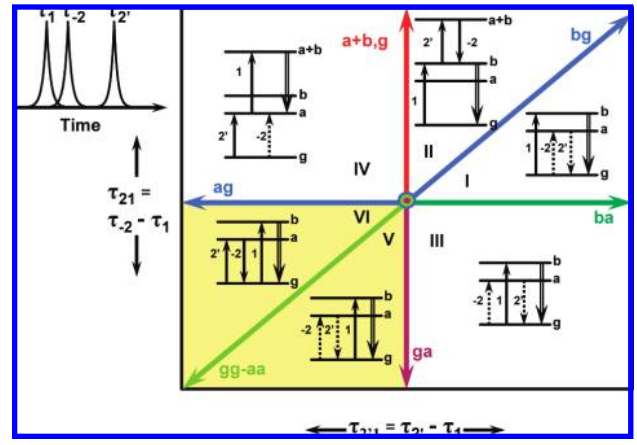

FIGURE 4. Schematic diagram showing coherence pathways for time orderings I−VI of three excitation pulses. Colored arrows indicate direction for coherence dephasing or population decay. Colors correlate with specific nonlinear processes. Adapted from ref 2.

Coherence and Population Dynamics

Fixing the excitation and monochromator frequencies and scanning the time delays between pulses 2, 2′, and 1 ($\tau_{2'1}$ and τ_{21}) accesses all 12 pathways in Figure 1. Figure 4 represents this procedure.[2] The upper left shows three pulses with the time ordering 1, −2, and 2′ corresponding to region labeled I. There are five other time orderings (labeled II−VI[2]) shown along with a fully resonant WMEL diagram. There is also a second pathway (not shown) for each time ordering. (The fully resonant pathways shown for time ordering I−VI in Figure 4 correspond to pathways 1A, 2A, 3A, 4B, 5A, and 6A, respectively, in Figure 1. The pathways that are not shown for time orderings I−VI correspond to pathways 1B, 2B, 3B, 2A, 5B, and 6B, respectively, in Figure 1.) The arrows along each axis define the coherence or population that is changing in the direction of the arrow. For example, the red arrow indicates that the (*a*+*b*,*g*) double quantum coherence is decaying along the indicated direction as τ_{21} increases with $\tau_{2'1}$ constant.

There is a correspondence between each region and different nonlinear techniques. For example, the maroon arrow is the time ordering for photon echo, the green and olive arrows are transient grating, the olive arrow is pump−probe, the red arrow is reverse photon echo (or equivalently HMQC), and the blue arrows are reverse transient grating.[17] Region V is the stimulated photon echo (the stimulated photon echo is a three pulse photon echo involving three pathways; the one shown in region V of Figure 4 is the bleaching pathway)

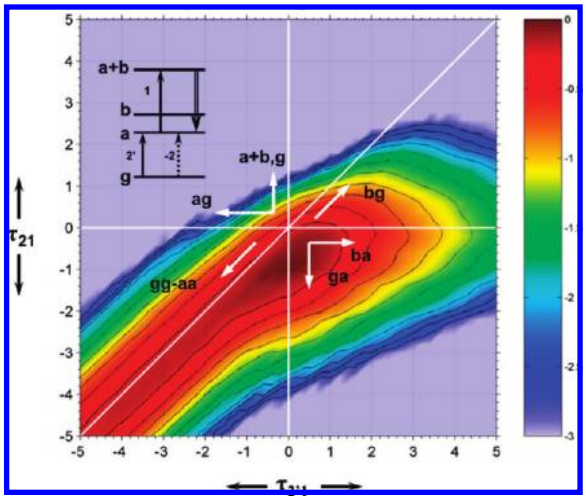

FIGURE 5. Intensity dependence (logarithmic) on the excitation pulse time delays for (ω_1, ω_2, ω_m) = (2002, 1943, 2002) cm^{-1}. White arrows indicate direction for coherence dephasing or population decay. The example WMEL diagram shows pathway IV (Figure 4). Adapted from ref 2.

method of 2D-IR, and region VI is the nonrephasing counterpart. The yellow region designates pathways with intermediate populations.

The experimental implementation of Figure 4 is shown in Figure 5, along with an example WMEL diagram for region IV. Again, arrows indicate the decaying coherences or populations. Here, ω_1, ω_2, and ω_m are tuned to the symmetric and asymmetric CO stretch modes (labeled *b* and *a*, see Table 1) representing the lower right Ni(CO)$_2$ cross peak in Figure 2a−c. Note that the maximum intensity is not symmetric across the diagonal axis since the intensity for pathway V is higher than that for pathway VI. Since the Ni(CO)$_2$ sample is inhomogeneously broadened and pathway V is a rephasing pathway, an echo is created that increases the pathway V intensity. This effect is the three pulse echo peak shift (3PEPS) used to measure the time correlation function of solvent and biological systems.[33]

Figure 5 contains the information for the dephasing rates of the *ag* (or *ga*) and *bg* single quantum coherences, the *ba* zero quantum coherence, and the relaxation rate of the *gg* − *aa* population difference. The (*a*+*b*,*g*) double quantum coherence is not represented because the choice of excitation and monochromator frequencies does not enhance pathways containing (*a*+*b*,*g*). Figure 6 shows four examples of scanning delay times $\tau_{2'1}$ and τ_{21} for fixed (ω_1, ω_2, ω_m). Figure 6a is identical to Figure 5 except the frequencies are interchanged to excite the upper left Ni(CO)$_2$ cross peak. This figure contains the same information as Figure 5 except the *a* and *b* designations are interchanged. Figure 6b results when (ω_1, ω_2, ω_m) are tuned to excite the lower right Ni(CO)$_2$ peak in Figure 2d. Although Figure 2d used the pathway IV time ordering, time orderings V and VI have nonparametric pathways with the same resonance conditions. Thus, pathways IV, V, and VI all contribute in Figure 6b. These pathways probe the (*a*+*b*,*g*) coherence dephasing time. Figure 6c results when the frequencies are tuned to excite pathway II. The other pathways are suppressed. Pathway II provides a second measure of the (*a*+*b*,*g*) coherence dephasing time. Finally, Figure 6d results when the frequencies are tuned to excite the nonparametric pathways of time orderings I−III (these pathways correspond to 1−3B in Figure 1). These pathways cannot be fully resonant with two tunable excitations because the four transitions have different frequencies. When the monochromator and excitation frequencies are tuned to maximize these pathways, the ω_2 frequency lies between the fundamental and the overtone or combination band frequencies, while the ω_1 frequency excites a fundamental transition.[31] The pathways for time orderings I−III are now excited and IV−VI are suppressed. Together, these experiments provide an overdetermined data set for defining the dephasing and relaxation dynamics of all the coherences and populations.

Hybrid Frequency-/Time-Domain Spectra

The excitation and monochromator frequencies and the excitation delay times form a multidimensional space, which is visualized with two-dimensional cross sections.[34] The examples thus far have largely involved scanning either the excitation frequencies or the delay times. Two-dimensional scans where both change can also be useful in resolving and defining relationships between spectral features. Figure 7 shows an example where the $\omega_1 = \omega_m$ is resonant with the symmetric CO stretch of Ni(CO)$_2$ at 2002 cm^{-1}, τ_{21}= 2 ps, and ω_2 and $\tau_{2'1}$ are scanned. The WMEL diagrams for the two peaks are also shown. The $\tau_{2'1}$ scan is a horizontal section of Figure 4 that covers regions I and II. The ω_2 scan is a vertical slice of Figure 2a in the region of the lower right Ni(CO)$_2$ cross peak. Two peaks appear at positions corresponding to the zero quantum *ba* coherence created by the *bg* → *ba* transition of pathway I and the double quantum *a*+*b*,*g* coherence created by the *bg* → *a*+*b*,*g* transition of pathway II. The $\tau_{2'1}$ delay times that maximize the two peaks are the same as the horizontal slices through τ_{21} = 2 ps in Figure 5 and Figure 6c, respectively. The peak separation along ω_2 defines the combination band.

Two dimensional cross sections that vary the excitation and monochromator frequencies display the relationships between the excitation and the output frequencies. Both the driven and free induction decay processes determine the output fre-

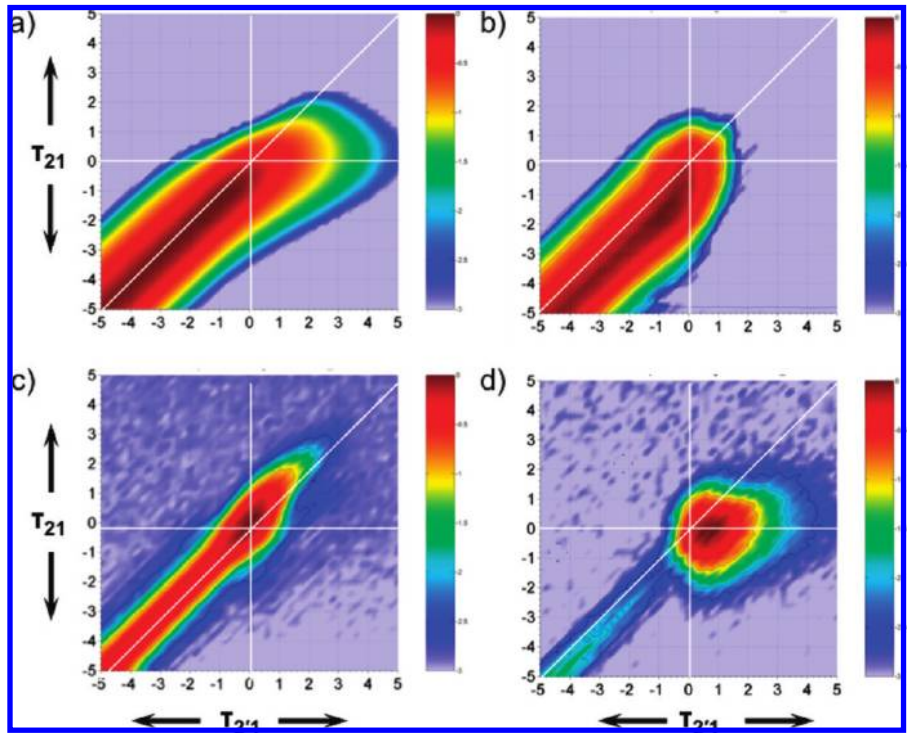

FIGURE 6. TRIVE FWM intensity dependence (logarithmic) on the excitation pulse time delays for the frequencies (ω_1, ω_2, ω_m) = (a) (1943, 2000, 1943) cm^{-1}, (b) (1982, 1943, 1982) cm^{-1}, (c) (2003, 1923, 2002) cm^{-1}, and (d) (2002, 1930, 1982) cm^{-1}. Adapted from ref 2.

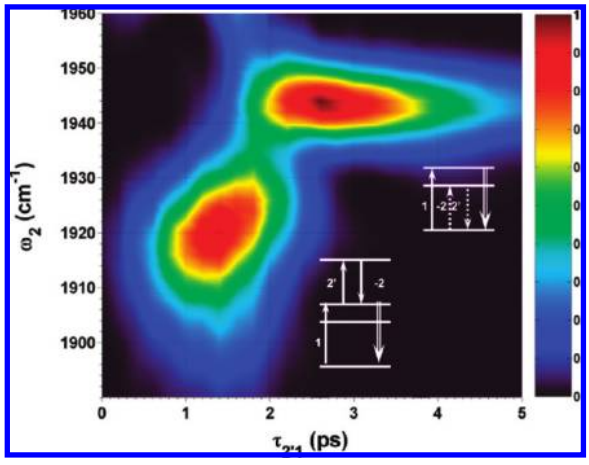

FIGURE 7. TRIVE FWM intensity dependence (linear) on ω_2 and $\tau_{2'1}$ when $\omega_1 = \omega_m = 2002$ cm^{-1} and τ_{21}= 2 ps and example WMEL diagrams for pathways I and II.

quency. Figure 8 shows four examples of these scans, all with ω_2 resonant with the C=O asymmetric mode at 1943 cm^{-1}. Figure 8a shows a typical scan for $\tau_{2'1} = 2$ and $\tau_{21} = 1$ ps, as well as an example WMEL diagram for this time ordering (region I in Figure 4). The peak appears when ω_1 and ω_m match the $g \leftrightarrow b$ fundamental transition as expected for the phase matching condition $\vec{k}_{signal} = \vec{k}_1 - \vec{k}_2 + \vec{k}_{2'}$ and the IA pathway. The peak is narrower along the ω_m axis because the monochromator resolution is higher than the spectral width of the excitation pulse. In addition, the monochromator measures both the FID defined by the dephasing rate and the driven signal defined by the excitation pulse widths.

Figure 8b shows the same plot for $\tau_{2'1} = \tau_{21} = 2$ ps. This time ordering corresponds to regions I and II. The example WMEL diagram corresponds to pathway IIB. The previous peak is still present, but a new feature appears when ω_m measures the $a+b \rightarrow a$ transition of pathways IB and IIB. These two pathways can only be doubly resonant with two tunable excitation pulses. Besemann et al. identify the resonances expected for these doubly resonant pathways.[34] Since ω_2 is resonant with the $g \rightarrow a$ fundamental transition, either ω_1 is resonant with the $g \rightarrow b$ fundamental transition or $\omega_1 + \omega_2$ is resonant with the $g \rightarrow a+b$ transition. Figure 8b shows that these pathways are efficiently excited at these two values of ω_1 as well as those in-between.

Figure 8c shows the same plot for $\tau_{2'1} = -1$, $\tau_{21} = 1$ ps along with an example WMEL diagram for pathway IVA. The region IV time ordering involves a double quantum coherence. The brightest peak corresponds to the fully resonant pathway IVB (shown in Figure 4) where ω_2 is resonant with the $g \rightarrow a$ transition, ω_1 is resonant with the $a \rightarrow a+b$ transition, and ω_m measures the $a+b \rightarrow a$ transition. Pathway IVA can only be doubly resonant with two tunable excitation pulses. There are three choices for ω_1 and ω_m that establish double resonances: (ω_1, ω_m) = (1976, 1976), (1976, 2002), and

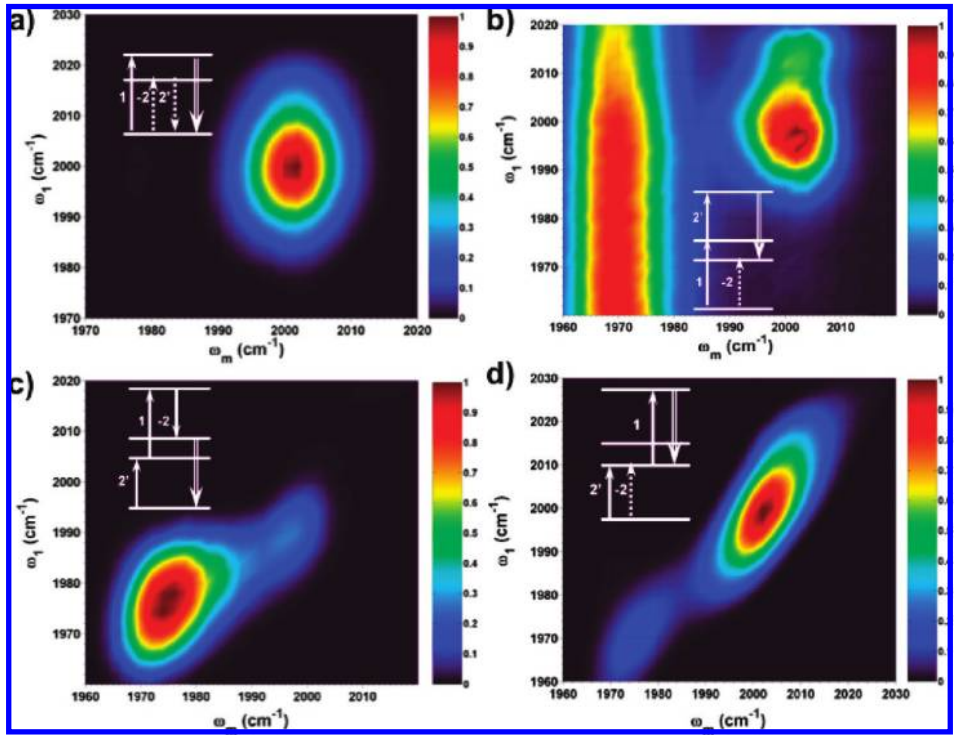

FIGURE 8. TRIVE FWM intensity dependence (linear) on ω_1 and ω_m when ω_2= 1943 cm^{-1} and ($\tau_{2'1}$, τ_{21}) are (a) (2, 1) ps, (b) (2, 2) ps, (c) (−1, 1) ps, and (d) (−2, −1) ps. These conditions emphasize pathways (a) I, (b) I and II, (c) IV, and (d) VI. Representative WMEL diagrams are also shown.

(2002, 2002) cm^{-1}. The resonant transitions and monochromator setting for the three cases are (1) $g \rightarrow a$, $a \rightarrow a+b$, driven process; (2) $g \rightarrow a$, $a \rightarrow a+b$, FID; (3) $g \rightarrow a$, $b \rightarrow g$, FID + driven process. The weak diagonal feature in Figure 8c is the observed consequence of these three processes occurring coherently and simultaneously.

Figure 8d shows the last example for $\tau_{2'1} = -2$, $\tau_{21} = -1$ ps and an example WMEL diagram for pathway VIB. The time ordering for region VI includes an intermediate population. The brightest peak corresponds to the fully resonant pathway VIA (see Figure 4) where ω_1 is resonant with the $g \rightarrow b$ transition, ω_2 is resonant with the $g \rightarrow a$ transition, and the monochromator measures the $g \rightarrow b$ transition. The weaker peak corresponds to the fully resonant pathway VIB where ω_1 is resonant with the $a \rightarrow a+b$ transition, ω_2 is resonant with the $g \rightarrow a$ transition and the monochromator measures the $a+b \rightarrow a$ transition. In both cases, the FID and driven processes both contribute. Note that the peaks have diagonal character. The driven process creates its output when $\omega_1 = \omega_m$, but the FID creates the output at the $\omega_m = b \rightarrow g$ or $a+b \rightarrow a$ transition. The observed peak appears along a diagonal between the expected positions of the FID and driven process.

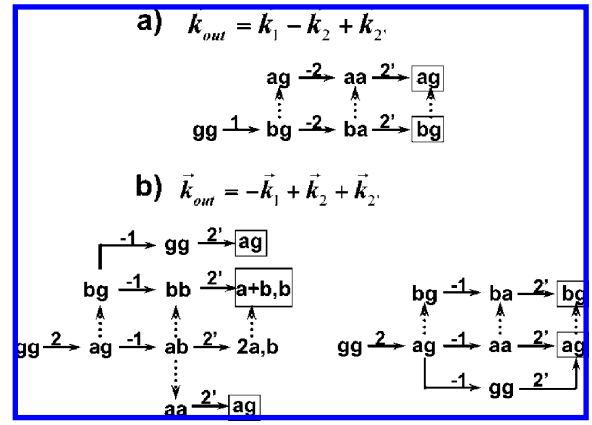

FIGURE 9. Representative coherence transfer pathways for two different phase matching conditions. The dotted arrows represent coherence transfer transitions. The emitting coherences are in boxes.

Coherence Transfer

Coherence transfer results when the thermal bath causes a superposition state such as *bg* to evolve to an *ag* coherence or vice versa.[35] It is the amplitude level analogue of population relaxation where a *bb* population decays to an *aa* population. Figure 9a shows the Liouville diagrams for the coherence transfer in pathway I of Figure 4. The pathway $gg \rightarrow bg \rightarrow ba \rightarrow bg$ represents the coherences responsible for creating the normal *bg* output coherence characteristic of pathway I. However, when the monochromator scans over all

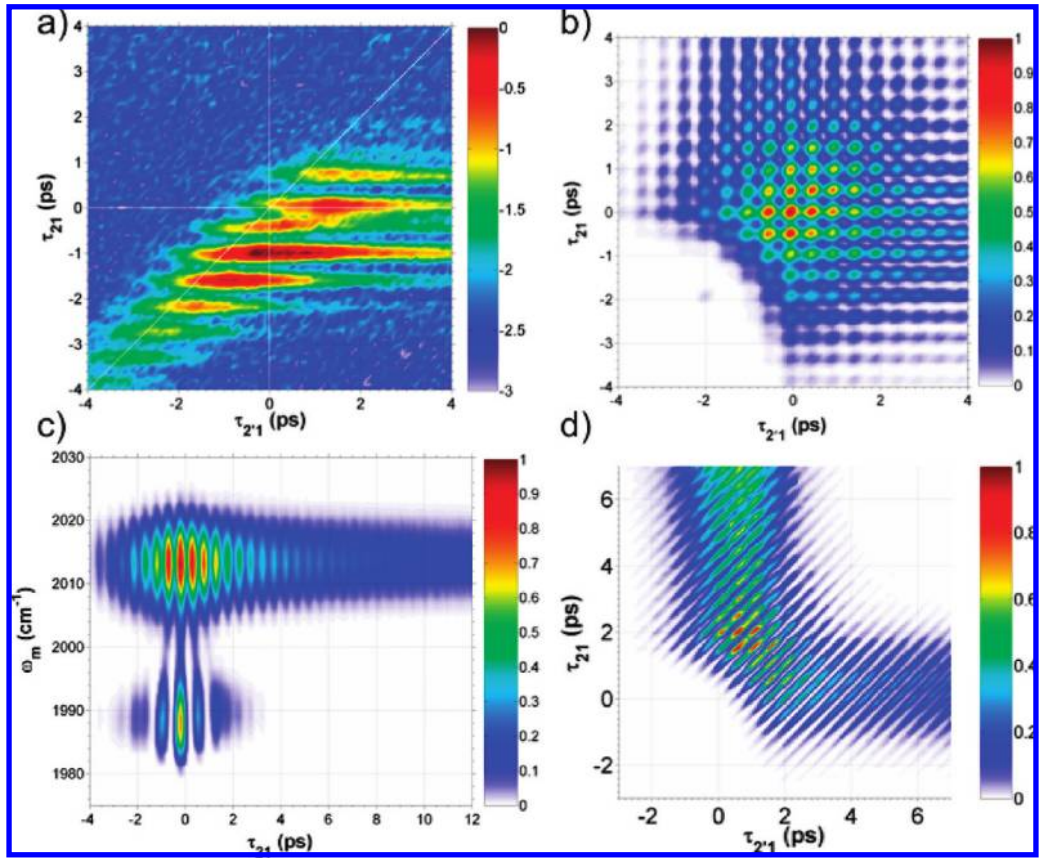

FIGURE 10. Examples of the temporal modulations caused by coherence transfer. Adapted from refs 40−42. (a) Time delay scan of $\tau_{2'1}$ and τ_{21} for $Ni(CO)_2$ exciting lower right cross-peak in Figure 2 using $(\omega_1, \omega_2, \omega_m) = (2002, 1943, 1943)$ cm^{-1} with $\vec{k}_{out} = \vec{k}_1 - \vec{k}_2 + \vec{k}_{2'}$. (b) Time delay scan of $\tau_{2'1}$ and τ_{21} for rhodium dicarbonyl acetylacetonate ($Rh(CO)_2$) exciting a cross-peak at $(\omega_1, \omega_2, \omega_m) = (2084, 2015, 2015)$ cm^{-1} with $\vec{k}_{out} = -\vec{k}_1 + \vec{k}_2 + \vec{k}_{2'}$. (c) Scans of τ_{21} and ω_m for $Rh(CO)_2$) with $(\omega_1, \omega_2) = (2084, 2015)$ cm^{-1} with $\vec{k}_{out} = -\vec{k}_1 + \vec{k}_2 + \vec{k}_{2'}$. (d) Time delay scan of $\tau_{2'1}$ and τ_{21} for $Rh(CO)_2$ exciting a diagonal peak at $(\omega_1, \omega_2, \omega_m) = (2015, 2015, 2084)$ cm^{-1} with $\vec{k}_{out} = -\vec{k}_1 + \vec{k}_2 + \vec{k}_{2'}$.

output frequencies, a weaker output signal is observed from the *ag* coherence.[36] This coherence can be created by coherence transfer as indicated by dotted lines in Figure 9a. Note there are three equivalent pathways involving coherence transfer in this time ordering. The *bg* and *ag* coherences oscillate at different frequencies and cause modulation when one feeds the other. Since the three pathways are equivalent, their amplitudes interfere with each other and cause a beating in the output coherence. Similar pathways occur for the other time orderings as well. If one now repeats the experiment shown in Figure 5 but with the monochromator tuned to the coherence transfer peak, Figure 10a results. It is very similar to Figure 5 except now there are strong modulations that are characteristic of the interference between the pathways.[36] The frequency difference between the two coherences involved in the transfer defines the modulation's period.

This experiment used the phase matching condition $\vec{k}_{signal} = \vec{k}_1 - \vec{k}_2 + \vec{k}_{2'}$ where the normal output is much brighter than the output created by coherence transfer. However, if the phase matching condition is $\vec{k}_{signal} = -\vec{k}_1 + \vec{k}_2 + \vec{k}_{2'}$, the normal output for this pathway is forbidden while the output created by coherence transfer is allowed.[37] Figure 9b shows two sets of coherence transfer pathways for this phase matching condition. For the one on the left, the 2*a*,*b* output coherence resulting from three interactions requires a forbidden transition from an overtone state of one mode to the fundamental of another mode. However, coherence transfer creates either an *a*+*b*,*b* or *ag* coherence, both of which create allowed transitions. The normal output and the coherence transfer output now appear with similar intensities. Figure 10b shows the time delay scans when the monochromator monitors the *a*+*b*,*b* transition in a rhodium dicarbonyl chelate ($Rh(CO)_2$).[37] The modulations again appear because of the interference between the different equivalent pathways and the beating of the two coherences involved in the transfer. Again, the frequency difference between the two coherences defines the modulation period. Figure 10c shows a hybrid scan of the same material where both the monochromator and τ_{21} delay time are scanned. This plot shows both the *a*+*b*,*b* and *ag*

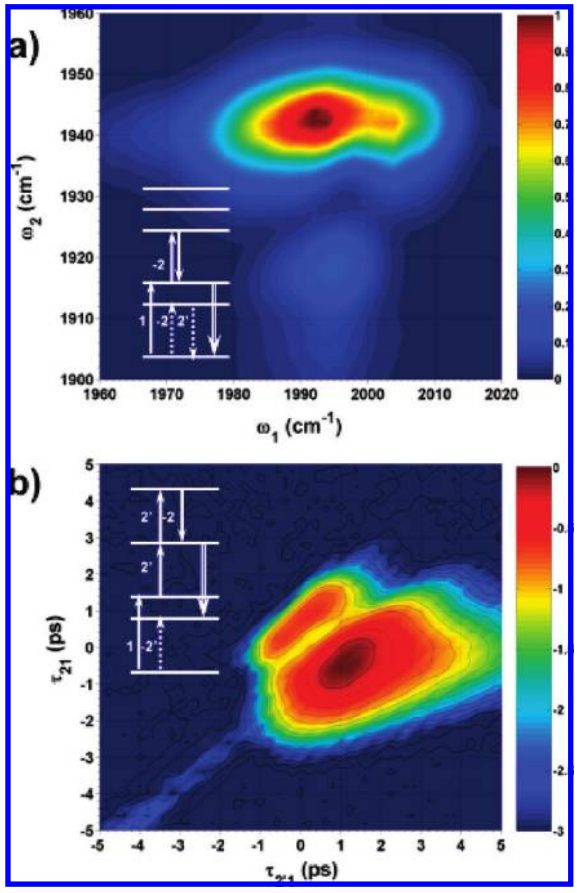

FIGURE 11. Changes when the excitation intensity is raised and higher order processes become important. (a) TRIVE FWM 2D spectrum scanning ω_1 and ω_2 near the $Ni(CO)_2$ with ω_m= 2002 cm^{-1} and ($\tau_{2'1}$, τ_{21}) = (2, 1) ps (pathway IA). (b) $\tau_{2'1}$ and τ_{21} scan with (ω_1, ω_2, ω_m) = (2002, 1931, 1982) cm^{-1}.

coherence output signals and the temporal modulations resulting from the coherence transfer.

Coherence transfer can also be used with single frequency excitation beams to discover states that are coupled to the resonant state.[38] The right side of Figure 9b shows the coherence transfer pathways when both ω_1 and ω_2 are tuned to the $g \rightarrow a$ transition. Coherence transfer to the coupled states now creates a *bg* coherence and a new output frequency. Monitoring this frequency in the $Rh(CO)_2$ chelate and scanning the time delays produces the modulations in Figure 10d characteristic of the interference between the coherence transfer pathways.

Higher Order Wave Mixing

What lies in the future? In NMR, selectivity is improved by establishing higher order multiple quantum coherences using higher order wave mixing (HOWM). In CMDS, each interaction is equivalent to an excitation pulse so multiple pulse methods require higher order wave mixing. Ivanecky and Wright explored using higher order wave mixing when the excitation intensities create Rabi frequencies that are comparable to or larger than the dephasing rates so more transitions can occur within the sample dephasing time.[22] Figure 11 shows two examples of raising the excitation intensities, still using the $\vec{k}_{out} = \vec{k}_1 - \vec{k}_2 + \vec{k}_{2'}$ phase matching condition. Figure 11a shows the effects of higher intensity for a time ordering in region I and the monochromator monitoring the fundamental $b \rightarrow g$ transition. Note the splitting that appears because of the dynamic Stark effect where the pathway

$$gg \xrightarrow{1} bg \xrightarrow{-2} ba \xrightarrow{2'} bg$$

becomes[39−41]

$$gg \overset{1}{\leftrightarrow} bg \overset{-2}{\leftrightarrow} ba \overset{2'}{\leftrightarrow} bg$$

A new peak appears because of new pathways such as

$$gg \xrightarrow{1} bg \xrightarrow{-2} ba \xrightarrow{+2} (a + b, a) \xrightarrow{-2} (b, a) \xrightarrow{2'} bg$$

Figure 11b shows an example of how the excitation intensity affects the delay time plots. Comparing with Figure 6d shows a node between regions I and II. This node results because a SWM pathway like

$$gg \xrightarrow{1} bg \xrightarrow{2'} (a + b, g) \xrightarrow{-2'} (a + b, a) \xrightarrow{2'}$$

$$(2a + b, a) \xrightarrow{-2} (a + b, a)$$

has the opposite sign from a pathway like

$$gg \xrightarrow{1} bg \xrightarrow{-2} ba \xrightarrow{2'} (a + b, g)$$

so destructive interference occurs. These observations demonstrate that HOWM is feasible. Using phase matching conditions like Ivanecky and Wright[22] will allow isolation of the HOWM.

Conclusions

This Account demonstrates how mixed frequency-/time-domain CMDS isolates the spectral features associated with interactions that couple quantum states, resolves spectral features, and measures their dynamics. It also provides examples of the range of behaviors that are possible with CMDS. It is still too early to answer the question of how widely CMDS will be used for analytical measurements and the types of methods that

will be used. Since frequency-domain CMDS requires only short-term phase coherence, one can use all of the fully coherent and population pathways and access all of the electronic and vibrational quantum states, regardless of the energy ranges. One is limited only by the laser technology. The detection limits may also be excellent. DOVE FWM involved very weak combination bands and double resonances. TRIVE FWM involves much stronger absorption strengths and triple resonances so their inherent nonlinearities are ~50× larger than DOVE FWM (~3×10^{-14} cm^3/erg for DOVE FWM vs ~2×10^{-12} cm^3/erg for TRIVE FWM).[42] Furthermore, typical intensities approach those required for saturation so the induced transition moment is comparable to single-molecule fluorescence. What then is preventing single-molecule CMDS? The excitation duty cycle is. A fluorescence experiment achieves single-molecule detection limits by continuous excitation, so the duty cycle is ~100%, while a CMDS experiment measures the emission for ~1 ps at a 1000 Hz repetition rate, so the duty cycle is 10^{-9}. Clearly, there is much room for improvement. Nevertheless, the promise is great, and the challenges are exciting.

This work was supported by the National Science Foundation under Grant CHE-0650431. We are grateful for the pioneering work of Roger Carlson, Kent Meyer, Wei Zhao, David Thompson, Daniel Besemann, Nicholas Condon, Mitchell LaBuda, James Hamilton, Peter Chen, Gregory Hurst, Joseph Ivanecky, Jack Steehler, Michael Riebe, Bruce Winker, Bradford Price, Dinh Nguyen, Steve Lee, and many former students in making CMDS a reality.

BIOGRAPHICAL INFORMATION

Andrei V. Pakoulev is an Assistant Scientist at UW—Madison. He received his M.S. in physics from Moscow Institute of Physics and Technology and his Ph.D. from Moscow State University with Nikolai Koroteev and Alexander Shkurinov and did postdoctoral research at University of Illinois with Dana Dlott. His research interests include development of nonlinear spectroscopic techniques to investigate coherent and incoherent intramolecular relaxation dynamics.

Mark A. Rickard is currently a research scientist at Dow Chemical Corporation. He received his B.S. from DePauw University and his Ph.D. at the University of Wisconsin, working in the Wright group on coherence transfer and quantum beating.

Kathryn M. Kornau received her B.S. in chemistry and Asian studies from St. Olaf College. After studying at Shanghai University of Traditional Chinese Medicine on a Fulbright Scholarship, she enrolled at the University of Wisconsin and worked in the Wright research group on developing TRIVE FWM.

Nathan A. Mathew received a B.S. in chemistry from the University of California, Irvine, and is currently a Ph.D. candidate in physical chemistry at the University of Wisconsin, Madison. His research focuses on extending the current methods and capabilities of coherent multidimensional vibrational spectroscopy.

Lena A. Yurs received a B.A. in chemistry and mathematics from Lakeland College in Sheboygan, WI. She worked with Ingrid Fritsch at the University of Arkansas—Fayetteville. She is a third year physical chemistry graduate student with John Wright studying higher-order wave mixing and its applications to novel systems.

Stephen B. Block graduated from Hanover College in southern Indiana in 2006, where he studied chemistry and mathematics. He is currently engaged in the development of IR-FWM at Wisconsin. He is studying charge transfer in semiconductors.

John C. Wright is the Andreas C. Albrecht Professor of Chemistry at the University of Wisconsin, Madison. He received his Ph.D. in Physics from Johns Hopkins University. His research program has focused on developing new analytical spectroscopies based on lasers. He began developing coherent multiresonant laser methods in 1978 and has applied them to a wide range of electronic and vibrational spectroscopy problems.

REFERENCES

1 Grzesiek, S.; Ikura, M.; Clore, G. M.; Gronenborn, A. M.; Bax, A. A 3d Triple-Resonance NMR Technique for Qualitative Measurement of Carbonyl-H-Beta J Couplings in Isotopically Enriched Proteins. *J. Magn. Reson.* **1992**, *96*, 215–221.

2 Pakoulev, A. V.; Rickard, M. A.; Meyers, K. A.; Kornau, K.; Mathew, N. A.; Thompson, D. C.; Wright, J. C. Mixed Frequency/Time Domain Optical Analogues of Heteronuclear Multidimensional NMR. *J. Phys. Chem. A* **2006**, *110*, 3352–3355.

3 Jonas, D. M. Two-Dimensional Femtosecond Spectroscopy. *Annu. Rev. Phys. Chem.* **2003**, *54*, 425–463.

4 Scheurer, C.; Mukamel, S. Infrared Analogs of Heteronuclear Nuclear Magnetic Resonance Coherence Transfer Experiments in Peptides. *J. Chem. Phys.* **2002**, *116*, 6803–6816.

5 Wright, J. C. Coherent Multidimensional Vibrational Spectroscopy. *Int. Rev. Phys. Chem.* **2002**, *21*, 185–255.

6 Cho, M. In *Advances in Multi-Photon Processes and Spectroscopy*, 1st ed.; Lin, S. H., Villaeys, A. A., Fujimura, Y., Eds.; World Scientific: Singapore, 1999; Vol. 12, pp 1−72.

7 Hamm, P.; Lim, M.; DeGrado, W. F.; Hochstrasser, R. M. Stimulated Photon Echoes from Amide I Vibrations. *J. Phys. Chem. A* **1999**, *103*, 10049–10053.

8 Zanni, M. T.; Asplund, M. C.; Hochstrasser, R. M. Two-Dimensional Heterodyned and Stimulated Infrared Photon Echoes of N-methylacetamide-D. *J. Chem. Phys.* **2001**, *114*, 4579–4590.

9 Smith, A. W.; Cheatum, C. M.; Chung, H. S.; Demirdoven, N.; Khalil, M.; Knoester, J.; Tokmakoff, A. Two-Dimensional Infrared Spectroscopy of beta-Sheets and Hairpins. *Biophys. J.* **2004**, *86*, 619a–619a.

10 Kwak, K.; Zheng, J. R.; Cang, H.; Fayer, M. D. Ultrafast Two-Dimensional Infrared Vibrational Echo Chemical Exchange Experiments and Theory. *J. Phys. Chem. B* **2006**, *110*, 19998–20013.

11 Hamm, P.; Lim, M.; Hochstrasser, R. M. Structure of the Amide I Band of Peptides Measured by Femtosecond Nonlinear-Infrared Spectroscopy. *J. Phys. Chem. B* **1998**, *102*, 6123–6138.

12 Naraharisetty, S. R. G.; Kasyanenko, V. M.; Rubtsov, I. V. Bond Connectivity Measured via Relaxation-Assisted Two-Dimensional Infrared Spectroscopy. *J. Chem. Phys.* **2008**, *128*, 104502.

13 Wright, J. C.; Carlson, R. J.; Hurst, G. B.; Steehler, J. K.; Riebe, M. T.; Price, B. B.; Nguyen, D. C.; Lee, S. H. Molecular, Multiresonant Coherent Four Wave Mixing Spectroscopy. *Int. Rev. Phys. Chem.* **1991**, *10*, 349–390.

14 Asplund, M. C.; Zanni, M. T.; Hochstrasser, R. M. Two Dimensional Infrared Spectroscopy of Peptides by Phase-Controlled Femtosecond Vibrational Echoes. *Proc. Natl. Acad. Sci. U.S.A.* **2000**, *97*, 8219–8224.

15 Shim, S. H.; Strasfeld, D. B.; Fulmer, E. C.; Zanni, M. T. Femtosecond Pulse Shaping Directly in the Mid-IR Using Acousto-optic Modulation. *Opt. Lett.* **2006**, *31*, 838–840.

16 Lee, D.; Albrecht, A. C. *Advances in Infrared and Raman Spectroscopy*, 1st ed.; Wiley-Heyden: Chichester, U.K., 1985; Vol. 12.

17 Mukamel, S. *Principles of Nonlinear Optical Spectroscopy*; 1st ed.; Oxford University Press: New York, 1995.

18 Cervetto, V.; Helbing, J.; Bredenbeck, J.; Hamm, P. Double-Resonance versus Pulsed Fourier Transform Two-Dimensional Infrared Spectroscopy: An Experimental and Theoretical Comparison. *J. Chem. Phys.* **2004**, *121*, 5935–5942.

19 Khalil, M.; Tokmakoff, A. Signatures of Vibrational Interactions in Coherent Two-Dimensional Infrared Spectroscopy. *Chem. Phys.* **2001**, *266*, 213–230.

20 DeCola, P. L.; Andrews, J. R.; Hochstrasser, R. M.; Trommsdorff, H. P. Simultaneous Narrow-Line Raman Spectra of Ground and Excited Electronic States. *J. Chem. Phys.* **1980**, *73*, 4695–4696.

21 Lee, S. H.; Steehler, J. K.; Nguyen, D. C.; Wright, J. C. Site Selective Nonlinear Four Wave Mixing by MENS and MEPS. *Appl. Spectrosc.* **1985**, *39*, 243–253.

22 Ivanecky, J. E.; Wright, J. C. An Investigation of the Origins and Efficiencies of Higher-Order Nonlinear Spectroscopic Processes. *Chem. Phys. Lett.* **1993**, *206*, 437–444.

23 Zilian, A.; LaBuda, M. J.; Hamilton, J. P.; Wright, J. C. A New 4WM Process: Vibrationally Enhanced IR Spectroscopy. *J. Lumin.* **1994**, *60&61*, 655–657.

24 Wright, J. C.; Chen, P. C.; Hamilton, J. P.; Zilian, A.; LaBuda, M. J. Theoretical Foundations for a New Family of Infrared Four Wave Mixing Spectroscopies. *Appl. Spectrosc.* **1997**, *51*, 949–958.

25 Zhao, W.; Wright, J. C. Measurement of chi(3) for Doubly Vibrationally Enhanced Four Wave Mixing Spectroscopy. *Phys. Rev. Lett.* **1999**, *83*, 1950–1953.

26 Zhao, W.; Wright, J. C. Spectral Simplification in Vibrational Spectroscopy Using Doubly Resonant Infrared Four Wave Mixing. *J. Am. Chem. Soc.* **1999**, *121*, 10994–10998.

27 Zhao, W.; Wright, J. C. Doubly Vibrationally Enhanced Four Wave Mixing Spectroscopy- The Optical Analogue to 2D NMR. *Phys. Rev. Lett.* **2000**, *84*, 1411–1414.

28 Meyer, K. A.; Wright, J. C. Detection Limits of Doubly Vibrationally Enhanced Four Wave Mixing in CS2. *Anal. Chem.* **2001**, *73*, 5020–5025.

29 Meyer, K. A.; Wright, J. C. Interference, Dephasing, and Coherent Control in Time-Resolved Frequency Domain Two-Dimensional Vibrational Spectra. *J. Phys. Chem. A* **2003**, *107*, 8388–8395.

30 Meyer, K. A.; Besemann, D. M.; Wright, J. C. Coherent Two Dimensional Spectroscopy with Triply Vibrationally Enhanced Infrared Four Wave Mixing. *Chem. Phys. Lett.* **2003**, *381*, 642–649.

31 Meyer, K. A.; Thompson, D. E.; Wright, J. C. Frequency and Time Resolved Triply Vibrationally Enhanced Four Wave Mixing Spectroscopy. *J. Phys. Chem. A* **2004**, *108*, 11485–11493.

32 Pakoulev, A. V.; Rickard, M. A.; Mathew, N. A.; Kornau, K. M.; Wright, J. C. Spectral Quantum Beating in Mixed Frequency/Time-Domain Coherent Multidimensional Spectroscopy. *J. Phys. Chem. A* **2007**, *111*, 6999–7005.

33 Joo, T.; Jia, Y.; Yu, J. Y.; Lang, M. J.; Fleming, G. R. Third-Order Nonlinear Time Domain Probes of Solvation Dynamics. *J. Chem. Phys.* **1996**, *104*, 6089–6108.

34 Besemann, D. M.; Meyer, K. A.; Wright, J. C. Spectroscopic Characteristics of Triply Vibrationally Enhanced Four Wave Mixing Spectroscopy. *J. Phys. Chem. B* **2004**, *108*, 10493–10505.

35 Khalil, M.; Demirdoven, N.; Tokmakoff, A. Vibrational Coherence Transfer Characterized with Fourier-Transform 2D IR Spectroscopy. *J. Chem. Phys.* **2004**, *121*, 362–373.

36 Rickard, M. A.; Pakoulev, A. V.; Kornau, K.; Mathew, N. A.; Wright, J. C. Interferometric Coherence Transfer Modulations in Triply Vibrationally Enhanced Four-Wave Mixing. *J. Phys. Chem. A* **2006**, *110*, 11384–11387.

37 Rickard, M. A.; Pakoulev, A. V.; Mathew, N. A.; Kornau, K. M.; Wright, J. C. Frequency- and Time-Resolved Coherence Transfer Spectroscopy. *J. Phys. Chem. A* **2007**, *111*, 1163–1166.

38 Pakoulev, A. V.; Rickard, M. A.; Mathew, N. A.; Kornau, K. M.; Wright, J. C. Frequency-Domain Time-Resolved Four Wave Mixing Spectroscopy of Vibrational Coherence Transfer with Single-Color Excitation. *J. Phys. Chem. A* **2008**, *112*, 6320–6329.

39 Carlson, R. J.; Wright, J. C. Effects of Saturation on the Elimination of Inhomogeneous Broadening by Nondegenerate Fully Resonant Four-Wave Mixing. *J. Lumin.* **1987**, *38*, 331–332.

40 Winker, B. K.; Wright, J. C. Nonlinear Atomic Spectroscopy of Flames. *Anal. Chem.* **1988**, *60*, 2599–2608.

41 Winker, B. K.; Wright, J. C. Four Wave Mixing with Dynamic Stark Effects in Flames. *Opt. Lett.* **1989**, *14*, 54–56.

42 Besemann, D.; Condon, N.; Meyer, K.; Zhao, W.; Wright, J. C. Experimental Determinations of Coherent Multidimensional Vibrational Spectroscopy. *Bull. Korean Chem. Soc.* **2003**, *24*, 1119–1125 .